nature physics

Article

https://doi.org/10.1038/s41567-023-02210-4

Fluctuation-enhanced phonon magnetic moments in a polar antiferromagnet

Received: 2 September 2022

Accepted: 14 August 2023

Published online: 14 September 2023

Check for updates

Fangliang Wu[1,6], Song Bao[1,6], Jing Zhou[2,3], Yunlong Wang[1], Jian Sun[1,4], Jinsheng Wen[1,4] ✉, Yuan Wan[2,3,5] ✉ & Qi Zhang[1,4] ✉

Phonons are the quasiparticles of collective lattice excitations that may carry finite angular momenta, but commonly exhibit negligible magnetic moments. A large phonon magnetic moment enables the direct mutual control of magnetic orders and lattice motions, and could be applied to develop spin–phononic devices. In some non- and paramagnetic systems, a large phonon magnetic moment is found due to coupling with electronic excitations. However, for magnetically ordered systems, a correspondingly large moment has not yet been discovered, and the roles of many-body correlations and fluctuations in phonon magnetism remain unclear. Here we report a phonon magnetic moment that is enhanced by critical fluctuations in a polar antiferromagnet, namely, $Fe_2Mo_3O_8$. Combining magneto-Raman spectroscopy and inelastic neutron scattering measurements, we show that a pair of low-lying chiral phonons carry large magnetic moments. Once the system is driven to a ferrimagnetic phase, we observe a splitting between the chiral phonons of nearly a quarter of the phonon frequency. We also observe a sixfold enhancement in the phonon magnetic moment in the vicinity of the Néel temperature. A microscopic model based on the coupling between phonons and both magnons and paramagnons accounts for the experimental observations.

The interplay between phonons and magnetism has attracted a lot of attention from researchers[1–5]. Recent advances in the phononic control of spin dynamics[1,2] and macroscopic magnetization[3], as well as the magnetic tuning of phononic properties[4,5], have stimulated general interest in the fields of phono-magnetism and magneto-phononics[6], in analogy to opto-magnetism and magneto-optics, respectively, for photons. The discovery of chiral phonons with finite angular momenta[7–10] has also driven the search for large phonon magnetic moments (PMMs), which provide a direct link between lattice vibrations and magnetism, and can be exploited for developing spin–phononic devices.

An orbital PMM given by ionic cyclotron motions is very weak due to the large ion mass, typically on the order of 10^{-4} Bohr magneton (μ_B) (ref. 11). In some rare-earth paramagnets[12,13], large PMMs have been reported, where a Raman-type spin–phonon interaction couples the phonon with an electronic crystal-field transition of the rare-earth ions[14]. Recently, some peculiar non-magnetic materials have been found to exhibit large PMMs[15,16], where the coupling between phonons, electronic transitions and band structures may play a key role[15,17–19]. However, for magnetically ordered systems, despite their versatile spin–phonon interactions and long-range spin correlations, a large PMM has not yet been identified. It remains unclear what the general pathways are for phonons to acquire a magnetic moment in the presence of many-body correlations and fluctuations, and how the PMM would behave across a magnetic-phase transition, where the correlation changes from coherent to incoherent and from long range to short range.

[1]National Laboratory of Solid State Microstructures and Department of Physics, Nanjing University, Nanjing, China. [2]Institute of Physics, Chinese Academy of Sciences, Beijing, China. [3]University of Chinese Academy of Sciences, Beijing, China. [4]Collaborative Innovation Center of Advanced Microstructures, Nanjing University, Nanjing, China. [5]Songshan Lake Materials Laboratory, Dongguan, China. [6]These authors contributed equally: Fangliang Wu, Song Bao. ✉e-mail: jwen@nju.edu.cn; yuan.wan@iphy.ac.cn; zhangqi@nju.edu.cn

In parallel to the search for large PMMs, magnetic excitations with electric dipole activity, known as electromagnons, have been the subject of substantial effort from researchers[20–26]. An electromagnon couples much more strongly to light than a regular magnon via a magnetic-dipole transition. Although the microscopic mechanisms of electromagnons differ in various systems[22,24–26], spin–lattice interaction is believed to be one of the major driving forces[22–24]. It was shown that magnons can acquire electric dipole activity by coupling with phonons[22,27]. Yet, the conjugate scenario, where phonons can be endowed with large magnetic moments in multiferroics, remains unexplored.

Here we report the observation of critical fluctuation-enhanced PMMs in a collinear multiferroic insulator $Fe_2Mo_3O_8$. We find that the low-energy excitation at 42 cm^{-1} (5.3 meV) has a phononic origin, whereas it was previously thought to be an electromagnon. We trace it back to a pair of degenerate, Raman-active phonon modes in the high-temperature paramagnetic phase. The phononic nature of this excitation is further supported by inelastic neutron scattering (INS) measurements. Utilizing polarization-resolved magneto-Raman spectroscopy, we observe the Zeeman splitting of phonon modes with a PMM of 0.11μ_B in the low-temperature antiferromagnetic (AFM) phase. Once driving $Fe_2Mo_3O_8$ to the ferrimagnetic (FiM) phase by magnetic fields, the phonon modes with opposite chiralities exhibit a giant splitting of 1.25 meV, nearly a quarter of the phonon frequency. In the vicinity of the Néel temperature (T_N), a nearly 600% enhancement in the PMM (0.68μ_B) is observed. Our results pinpoint to spin correlations as the underlying mechanism for the large PMM in this system. We further flesh it out with a minimal model based on phonon–(para) magnon coupling, and identify the FiM fluctuation as the key ingredient for the critical enhancement in PMM.

$Fe_2Mo_3O_8$ is a collinear multiferroic insulator with the space group $P6_3mc$ (ref. 28). An AFM order forms below 60 K in $Fe_2Mo_3O_8$, accompanied by a change in the electric polarization along the c axis[29]. Previous studies have revealed the giant thermal Hall effect[30], the existence of electromagnons[31] and non-reciprocal terahertz transmission[32] in this system. As shown in Fig. 1a, $Fe_2Mo_3O_8$ features a magnetic lattice consisting of two types of Fe site, namely, the tetrahedron (Fe-I) and the octahedron (Fe-II), with different magnetic moments along the c axis[33]. Within each Fe layer, spins form an approximate honeycomb lattice with a Néel-type order, and carry a net magnetization due to the uncompensated magnetic moments from the two types of Fe site. The net magnetizations in adjacent Fe layers are staggered (Fig. 1a). A magnetic field along the c axis drives the system to an FiM phase where the net magnetizations are aligned for different Fe layers[29].

Figure 1c shows the Raman spectra of $Fe_2Mo_3O_8$ as a function of temperature. At 20 K, a prominent low-lying excitation is found at 42 cm^{-1} (5.3 meV), which matches the electromagnon reported in the terahertz or infrared (IR) measurements[31,34]. For brevity, we shall refer to the excitation at 42 cm^{-1} as the P1 mode in the ensuing discussions. In the IR studies, the electromagnon is visible only in the AFM phase and vanishes above T_N (refs. 31,34). By contrast, as shown in Fig. 1d, the P1 mode in the Raman spectra survives above the Néel temperature and remains well defined even at 300 K, which is five times higher than T_N. It excludes the possibility of P1 as a magnon or paramagnon. As the temperature increases, the frequency of the P1 mode exhibits a small blueshift when entering the paramagnetic phase, accompanied by a peak intensity drop and linewidth broadening from 0.7 to 4.0 cm^{-1}. The integrated Raman intensity of the peak remains in the same order of magnitude from 20 to 300 K. These observations suggest the P1 mode emerges from phonons, instead of spin excitations or crystal-field excitations. The unusual blueshift in P1 as a phonon will be subsequently explained.

The phononic nature of the P1 mode is further supported by first-principles calculations. The calculated lowest optical phonon is located at 58 cm^{-1}, which agrees well with the Raman scattering results. This Raman-active phonon mode is doubly degenerate with E_2 symmetry, and can be decomposed into a pair of phonons with opposite ionic cyclotron motions (Fig. 1b). In this phonon mode, the Fe-I ions exhibit much larger atomic displacement than the Fe-II ones, and have a π-phase shift in the displacements between the adjacent Fe layers. The atomic motions of all the atoms are mainly in the a–b plane. Supplementary Fig. 13 provides the details.

The INS measurements further confirm the phononic origin of the P1 mode. In neutron scattering, spin and lattice excitations can be differentiated by the trend of their scattering intensity as a function of wavevector Q. For spin excitations, the scattering intensity generally decreases with increasing Q due to the reduced magnetic form factor[35], whereas phonons may exhibit an opposite trend depending on their structure factors. As shown in Fig. 1f, a pronounced peak at around 5.3 meV (42 cm^{-1}) appears in the energy scan for Q = (1, 0, 1) at 6 K, which matches well with the P1 mode in the Raman spectra. The neutron scattering intensity of P1 exhibits a general trend of increase for higher Q within our measurement range, which is consistent with the calculated phonon structure factors (Supplementary Fig. 12). At 100 K, a temperature well above T_N, the P1 mode is buried under the paramagnon background for Q = (1, 0, 1), and becomes more visible at higher Q values. For Q = (2, 0, 4), the integrated neutron intensity of the P1 mode exhibits a 1.8 times increase at 100 K compared with that at 6 K, which is consistent with the ratio due to the Bose factor (2.3). The small reduction in the ratio is attributed to the additional magnetic scattering of the P1 mode at 6 K, which is also consistent with the Raman spectra (Supplementary Fig. 5). Thus, the observation of P1 above T_N in the INS spectra, as well as its Q dependence, provides compelling evidence for the P1 mode mainly being a phonon in both AFM and paramagnetic phases.

Having firmly established the phononic origin of the P1 modes, we unveil their PMM by performing polarization-resolved magneto-Raman spectroscopy with a c-axis magnetic field. Figure 2a presents the Raman spectra from −9 to +9 T excited by linearly polarized light. The peaks at 88 cm^{-1} (M1) and 113 cm^{-1} (M2) exhibit a linear splitting in energy. We identify them as the four AFM magnon branches[31,34]. Meanwhile, the P1 phonon peak broadens as the field increases. With cross-circular Raman scattering configurations, we resolve a clear linear splitting of P1 phonons under magnetic fields. The two cross-circular Raman scattering processes, namely, left-handed circular excitation and right-handed emission (LR) or right-handed excitation and left-handed emission (RL), have opposite angular momenta transfer between the light and the material, thereby providing information regarding the angular momentum carried by the excitation (Supplementary Fig. 6). The Raman scattering of the P1 phonon and AFM magnons mainly happens in cross-circular channels (Supplementary Fig. 7). Here we define the degree of circular polarization (DCP) of the Raman spectra as $(I_{LR} - I_{RL})/(I_{LR} + I_{RL})$, where I_{LR} (I_{RL}) is the Raman intensity in the LR (RL) channel. Figure 2a (bottom) presents the DCP spectra of the Raman scattering. A linear Zeeman splitting of the P1 phonons is clearly shown. The red and blue branches indicate excitations with opposite DCP and angular momenta.

Zeeman splitting provides a direct measure of the magnetic moment carried by a quasiparticle, which can be obtained from the energy difference between the split modes ($\mu = \Delta E/2B$, where μ, ΔE and B are the magnetic moment, Zeeman splitting energy and magnetic field, respectively). The measured magnetic moments of the M1 and M2 modes are 2.0μ_B and 2.4μ_B, respectively, consistent with their identification as magnons. For the P1 phonons, the splitting of 1 cm^{-1} at 9 T yields a PMM of 0.11μ_B. This value is three orders of magnitude larger than a regular orbital PMM[11]. As shown in Fig. 2b, the Stokes and anti-Stokes Raman scatterings of P1 phonons follow the opposite selection rules. It arises from the opposite photon-to-material angular momentum transfer of the two scattering processes. The observation of phonon Zeeman splitting together with their Raman selection rules prove that the doubly degenerate P1 modes consist of a pair of chiral phonons carrying opposite angular momenta and magnetic moments under magnetic fields.

https://doi.org/10.1038/s41567-023-02210-4

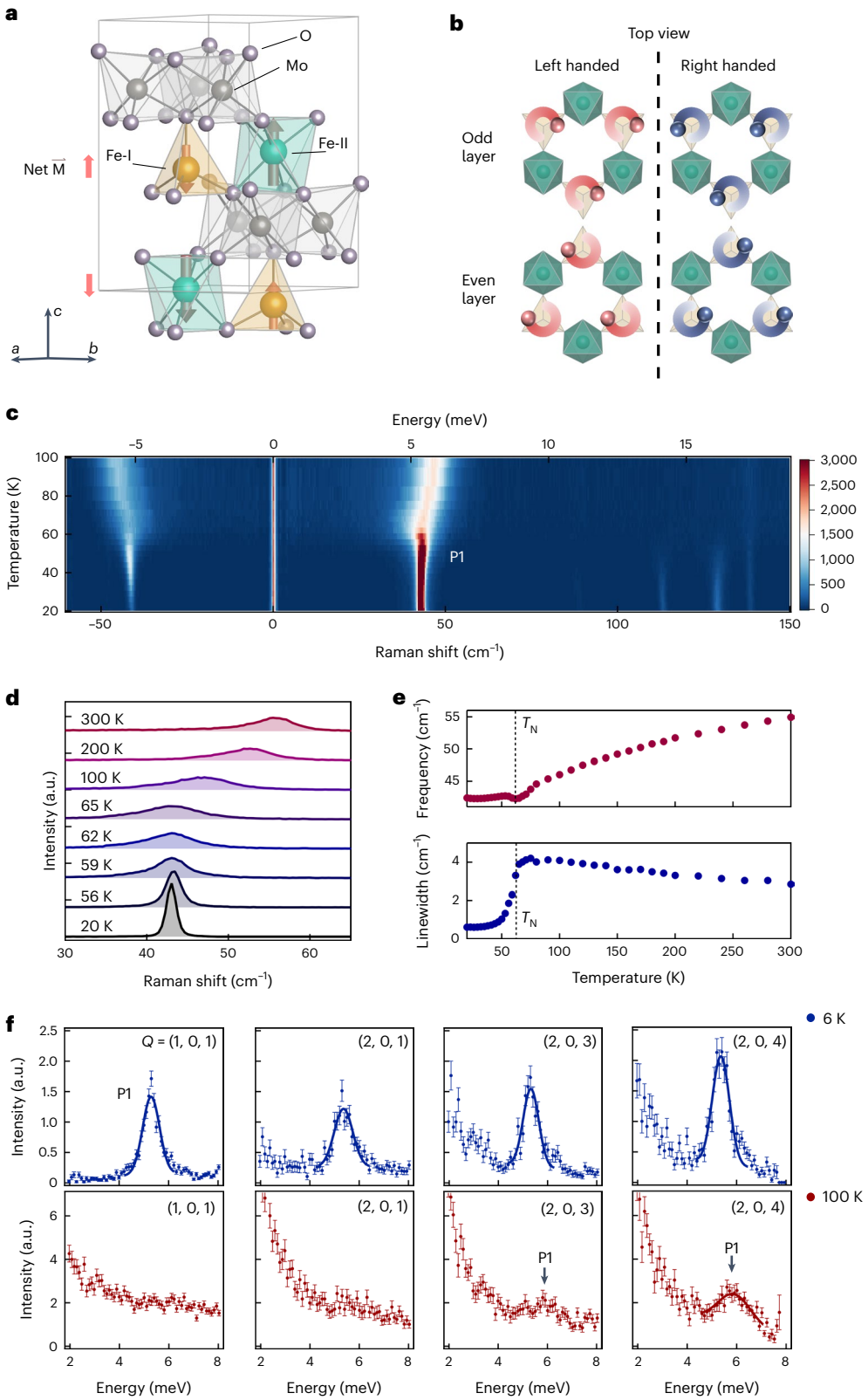

Fig. 1 | Low-lying phononic excitation in $Fe_2Mo_3O_8$. a, Schematic of the crystal structure of $Fe_2Mo_3O_8$. Two types of Fe site, namely, tetrahedron and octahedron, are marked as Fe-I and Fe-II, respectively. **b**, Schematic of the atomic displacements of P1 phonons based on first-principles calculations. The double-degenerate E_2 phonons can be decomposed into a pair of chiral phonons with opposite cyclotron motion of Fe ions, shown as left- and right-handed modes in the figure. **c**, Raman spectra of $Fe_2Mo_3O_8$ from 20 to 100 K. **d**, Raman spectra of the low-lying excitation at various temperatures up to 300 K. The P1 mode exists in the paramagnetic phase, and remains well defined even at 300 K, suggesting its phononic nature. **e**, Peak position of the P1 phonon as a function of temperature (top). The phonon blueshifts above the Néel temperature (T_N). Linewidth of P1 phonons from 20 to 300 K (bottom). The error bars are smaller than the symbols. **f**, INS energy scans of $Fe_2Mo_3O_8$ at a different wavevector Q at 6 and 100 K. The P1 mode is visible at both temperatures with its scattering intensity increasing with Q in general, indicating its phononic origin. The error bars represent one standard deviation.

https://doi.org/10.1038/s41567-023-02210-4

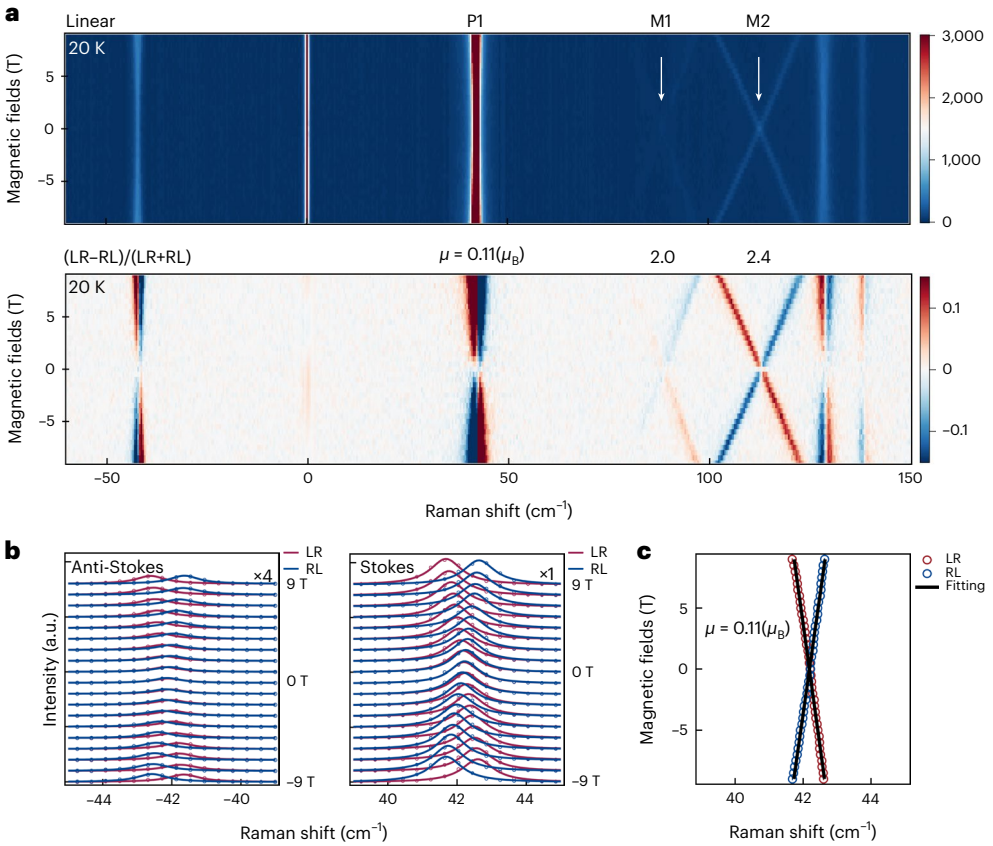

Fig. 2 | Large PMMs in $Fe_2Mo_3O_8$ revealed by magneto-Raman spectroscopy. **a**, Polarization-resolved magneto-Raman spectroscopy of $Fe_2Mo_3O_8$ from −9 to +9 T at 20 K. Magneto-Raman spectra under linearly polarized excitation and unpolarized detection (top). The Zeeman splitting of the two pairs of AFM magnons (M1 and M2) are observed. DCP of the Raman spectra in the cross-circular channels (bottom). The RL channel of Raman scattering represents right-handed excitation and left-handed detection, whereas LR represents the opposite scheme. The P1 phonon mode exhibits Zeeman splitting with a magnetic moment of $0.11\mu_B$. The measured magnetic moments of other excitations are also listed in the unit of Bohr magneton. **b**, Stokes and anti-Stokes Raman spectra of P1 phonons in the two cross-circular channels. The two Zeeman-split phonons exhibit opposite circular selection rules, indicating that they carry opposite phonon angular momenta. The polarization selection rules are also opposite for the Stokes and anti-Stokes Raman processes of P1. **c**, Peak positions of Zeeman-split P1 phonons with linear fitting.

The magnetic ground state of $Fe_2Mo_3O_8$ is AFM, which can be driven to FiM by a large magnetic field along the *c* axis[29]. In the FiM phase, the net magnetic moments of each Fe layer are aligned. The critical field of the AFM–FiM transition is beyond 10 T at 4 K and decreases at elevated temperatures[29]. Figure 3a presents the polarization-resolved magneto-Raman spectra of the P1 phonons at 49 K. A pair of new modes suddenly appear at 6.5 T, corresponding to the chiral P1 phonons in the FiM phase. The Raman intensity of the AFM P1 phonons is transferred to the FiM ones as the field increases. The co-existence of the two pairs of P1 modes at around 6.5 T is due to the co-existing AFM and FiM domains, which is a characteristic of a first-order phase transition. The pair of P1 phonons in the FiM phase possesses a giant energy splitting of 10 cm^{-1} (1.25 meV), nearly 24% of the phonon frequency, which is the largest reported ratio, to the best our knowledge. Similar to their AFM counterparts, the Raman scattering signals of the FiM P1 phonons are also dominated by the cross-circular channels. Chirality-selective Raman excitation of these phonons is achieved with circularly polarized light (Fig. 3a,b). At 52 K, the critical field of the AFM–FiM transition reduces to 4.5 T. The extracted peak positions of the P1 phonons at 49 K are shown in Fig. 3c. Figure 3d illustrates a map of P1 phonon splitting as a function of both temperatures and magnetic fields. The plateau of giant splitting over 1 meV coincides with the FiM phase in the phase diagram of $Fe_2Mo_3O_8$, which is independently determined by magnetization measurements.

The above observations show that the P1 phonons are Raman active in all of the AFM, FiM and paramagnetic phases. By contrast, their in-plane IR activity only appears in the AFM phase[31,34]. This is consistent with our symmetry analysis (Methods). Evidently, the P1 phonons carry the Raman-active E_2 representation of the point group 6*mm* in the paramagnetic phase, and carry the IR- and Raman-active *DE* co-representation of the 6′*m*′*m* magnetic point group in the AFM phase[36,37].

To further explore the interplay between PMM and magnetic order, we measure the temperature dependence of the Zeeman splitting of P1 phonons across the AFM–paramagnetic phase transition. Figure 4a presents the peak positions of chiral phonons as a function of magnetic fields at various temperatures. The PMMs of P1 modes in the AFM phase are extracted, whereas the FiM P1 modes are not included in this analysis. The spectra of chiral phonons at representative temperatures are shown in Fig. 4b. At a given magnetic field, the size of the phonon Zeeman splitting remains nearly constant below T_N; however, it exhibits a steep increase in the vicinity of T_N, further extending into the paramagnetic phase and finally vanishing at around 90 K. The extracted PMM exhibits a sixfold enhancement near T_N ($0.68\mu_B$) with respect to its low-temperature value ($0.11\mu_B$) (Fig. 4c).

We now discuss the mechanism for the large PMM in $Fe_2Mo_3O_8$. Given that $Fe_2Mo_3O_8$ exhibits an AFM order at low temperature, a natural mechanism is the magnon–phonon coupling. The magnons and P1 phonons have the same symmetry in the AFM phase and therefore can

https://doi.org/10.1038/s41567-023-02210-4

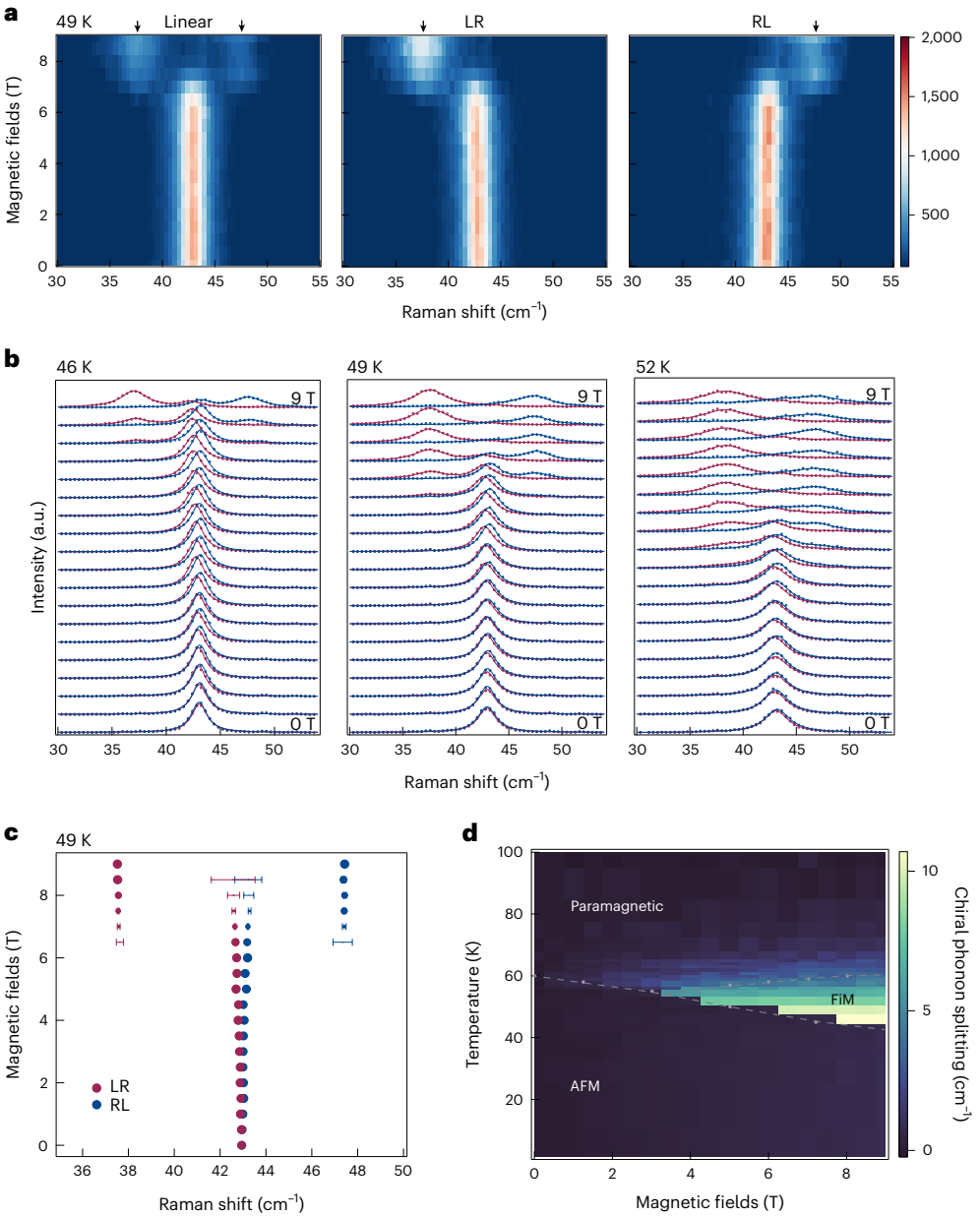

Fig. 3 | Giant chiral phonon splitting in the FiM phase of $Fe_2Mo_3O_8$. **a**, Polarization-resolved magneto-Raman spectra of $Fe_2Mo_3O_8$ at 49 K with linear, LR and RL polarization configurations. As the AFM–FiM transition happens at 6.5 T, a giant chiral phonon (P1) splitting appears. The P1 phonons in the FiM phase are marked by the arrows. **b**, Magneto-Raman spectra of P1 at 46, 49 and 52 K. The critical magnetic field reduces as the temperature increases. **c**, Peak positions of P1 in both AFM and FiM phases. The chiral phonon splitting reaches 10 cm^{-1} (1.25 meV), which is 24% of the phonon frequency. The size of the markers corresponds to the Raman intensity of each peak. The error bars represent the standard deviation. **d**, Map of chiral phonon splitting as a function of temperatures and magnetic fields. The area with the giant P1 phonon splitting matches with the FiM phase diagram of $Fe_2Mo_3O_8$. The grey dots mark the phase boundaries via independent magnetization measurements.

couple linearly. The coupling induces a hybridization between the two excitations, thereby endowing the phonons with a magnetic moment. To the leading order of the perturbation theory (Methods), the wavefunction of the P1 phonon mode acquires a magnon component whose magnitude is γ/Δ, where γ and Δ are the coupling strength and detuning between the two excitations, respectively. The PMM is, thus, given by $(\gamma/\Delta)^2\mu_{mag}$, where μ_{mag} is the magnon magnetic moment. As an order of magnitude estimate, we assume that the P1 phonon equally couples to the magnons, which yields $\gamma = 9.1$ cm^{-1} (1.1 meV). This mechanism qualitatively explains the unusual blueshift in P1 as the temperature goes beyond T_N. The phonon–magnon coupling renormalizes the energy of P1, and pushes it towards a lower energy with respect to its uncoupled value; hence, as the coupling eventually vanishes at high temperatures, the P1 mode recovers towards its bare frequency (Supplementary Fig. 3). Furthermore, this mechanism also explains the reduction in the neutron intensity of P1 at low Q in the paramagnetic phase. The slight phonon–magnon hybridization allows the P1 mode to scatter neutrons through not only the nuclear forces but also the magnetic dipolar interactions, especially at low Q. When such hybridization disappears at 100 K, consequently, the P1 mode loses this additional neutron cross section. This hybridization also explains the slight reduction in P1 intensity for $Q = (2, 0, 1)$ with respect to $(1, 0, 1)$ at 6 K, due to contributions from magnons.

Although the phonon–magnon coupling provides an explanation for the PMM at low temperatures, it must be extended to account for

https://doi.org/10.1038/s41567-023-02210-4

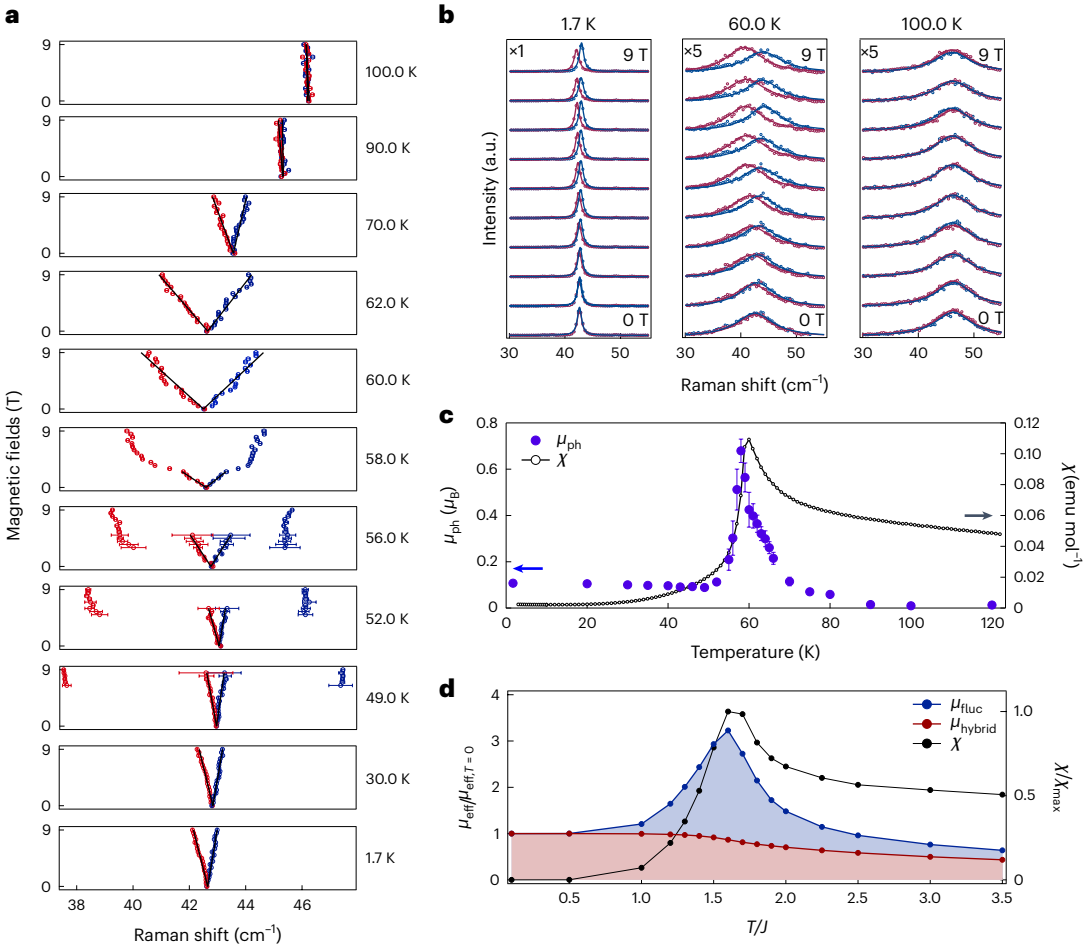

Fig. 4 | Critical fluctuation-enhanced PMMs near the temperature. a, Peak positions of the Zeeman-split P1 phonons as a function of magnetic fields and temperatures. The red and blue markers represent the peak positions of the two P1 phonons with opposite magnetic moments. The fitting lines of phonon Zeeman splitting are marked in black. The FiM P1 modes are not included in this analysis. The error bars represent one standard deviation. **b**, Magneto-Raman spectra of P1 phonons at the representative temperatures. The red and blue spectra are obtained under LR and RL polarization configurations, respectively. **c**, Measured PMMs and magnetic susceptibility (χ) as a function of temperatures. A sixfold enhancement in PMM is observed in the vicinity of T_N. In the paramagnetic phase, the temperature dependence of PMM deviates from the trend of magnetic susceptibility, and quickly decays to zero at around 90 K. The error bars represent one standard deviation. **d**, Simulated PMM (μ_{eff}) and magnetic susceptibility (χ) as a function of temperature (T). The μ_{eff} value is normalized against its value at zero temperature. The fluctuation enhancement in PMM near T_N is qualitatively reproduced. In the Monte Carlo simulation, we approximate $Fe_2Mo_3O_8$ as an Ising magnet with exchange energy J. Here $T_N = 1.6J$. We note that the paramagnons in the Ising model are local spin flips, which tend to be more robust against temperature. This leads to an overestimation of μ_{hybrid} and μ_{fluc} above T_N. It explains that the simulated PMM decreases more slowly with temperature than the experimental data. The error bars in **a** and **c** represent one standard deviation.

the dramatic enhancement in PMM near T_N. Hereafter, we argue that the FiM fluctuations are the other crucial ingredient for the enhanced PMM.

To set the stage, we note that each Fe layer in this material forms a ferrimagnet. The AFM and FiM phases exhibit the same type of FiM order within the layer and differ only in the direction of net magnetization between the layers. A moderate magnetic field or chemical substitution can drive the system from the AFM phase to the FiM phase. This suggests that we may view $Fe_2Mo_3O_8$ as weakly coupled FiM layers as a first approximation.

This picture explains the unusual behaviour of the magnetic susceptibility, which shows a sharp peak near T_N. Such sharp peaks are not expected for a conventional antiferromagnet such that the Néel order parameter does not linearly couple to the field. Here, as the temperature decreases, the system first develops FiM correlations within each layer. The susceptibility, thus, rapidly increases as in a ferrimagnet. Very close to T_N, the system establishes three-dimensional, AFM correlation due to interlayer coupling, which quenches the rapid growth of susceptibility.

Our picture implies that the system hosts FiM paramagnons above T_N. The phonon–paramagnon coupling can give rise to the phonon Zeeman effect similar to the phonon–magnon coupling. In the mean-field approximation, the Weiss molecular field associated with the FiM order has both spatially staggered and uniform components. The latter can act as an effective magnetic field and lead to phonon splitting akin to a genuine magnetic field. Its magnitude is $B' \approx Jm/\mu_B$, where J is the exchange-interaction energy scale and m is the FiM order parameter. Crucially, m is induced by the external field B and scales as $m \approx \chi' B$, where χ' is the susceptibility of the order parameter. The phonon Zeeman splitting is driven by the sum $B + B' = (1 + cJ\chi'/\mu_B)B$, where c is some numerical constant. Here χ' must be large at temperatures slightly above T_N due to the FiM correlation within the layers, which, in turn, gives rise to a large enhancement in the phonon Zeeman splitting and therefore the PMM.

Our picture also provides an intuitive explanation for the large phonon splitting in the FiM phase, where the order parameter m attains a finite value even when the external field B is extrapolated to zero. Consequently, the phonons exhibit a large splitting by molecular field B'.

We can make our picture concrete by constructing a minimal model, where we approximate $Fe_2Mo_3O_8$ as an Ising magnet (Methods). Our Monte Carlo simulation shows that this model can produce a sharp peak in magnetic susceptibility, indicative of FiM fluctuations above T_N (Fig. 4d). On incorporating a symmetry-allowed spin–phonon coupling, the model yields the phonon–(para)magnon coupling and therefore the PMM. We identify two contributions to the PMM, namely, $\mu_{eff} = \mu_{hybrid} + \mu_{fluc}$, where μ_{hybrid} is due to hybridization between the phonon and (para)magnons and μ_{fluc} is the part enhanced by the FiM molecular field. Figure 4d shows μ_{hybrid} and μ_{fluc} as functions of temperature for a representative phonon frequency. Although μ_{hybrid} monotonically decreases with increasing temperature due to the gradual loss of (para)magnon coherence, μ_{fluc} exhibits a sharp peak near T_N, reflecting the strong FiM fluctuations. We note that μ_{hybrid} decreases more slowly with temperature compared with the experimental data. This occurs because the paramagnons in the Ising model are local spin flips, which tend to be more robust against temperature and lead to an overestimation of μ_{hybrid} above T_N.

Taken together, we find that the low-lying doubly degenerate optical phonons in $Fe_2Mo_3O_8$ acquire large magnetic moments via the off-resonant coupling with magnons in the AFM phase. Enabled by the Néel-type spin order, these phonons become electric-dipole active below T_N. In the vicinity of the AFM–paramagnetic transition, the FiM fluctuations originating from the proximate FiM phase lead to a remarkable 600% enhancement in PMM. These discoveries present a new paradigm in the study of phonon magnetism, where the many-body correlations, instead of single-particle interactions, play key roles. It further establishes $Fe_2Mo_3O_8$ as an ideal platform for exploring phonon magnetism and developing hybrid phononic and spintronic devices in the terahertz regime. The P1 chiral phonons have both Raman and IR activity in the AFM phase. Meanwhile, their phonon chiralities and the associated magnetic moments can be selectively addressed by circularly polarized lights. These outstanding features pave the way for the coherent optical control of PMM in this system. Finally, our observations reveal the phononic origin of electromagnons in $Fe_2Mo_3O_8$, which shed new light on possible mechanisms for electromagnons and magneto-elastic excitations in other type-I multiferroics.

Online content

Any methods, additional references, Nature Portfolio reporting summaries, source data, extended data, supplementary information, acknowledgements, peer review information; details of author contributions and competing interests; and statements of data and code availability are available at https://doi.org/10.1038/s41567-023-02210-4.

References

1. Nova, T. F. et al. An effective magnetic field from optically driven phonons. *Nat. Phys.* **13**, 132 (2016).
2. Maehrlein Sebastian, F. et al. Dissecting spin-phonon equilibration in ferrimagnetic insulators by ultrafast lattice excitation. *Sci. Adv.* **4**, eaar5164 (2018).
3. Stupakiewicz, A. et al. Ultrafast phononic switching of magnetization. *Nat. Phys.* **17**, 489 (2021).
4. Huang, B. et al. Tuning inelastic light scattering via symmetry control in the two-dimensional magnet CrI_3. *Nat. Nanotechnol.* **15**, 212 (2020).
5. Jin, W. et al. Proc. Natl. Acad. Sci. U.S.A. **117**, 24664 (2020).
6. Juraschek, D. M., Narang, P. & Spaldin, N. A. Phono-magnetic analogs to opto-magnetic effects. *Phys. Rev. Research* **2**, 043035 (2020).
7. Zhang, L. & Niu, Q. Angular momentum of phonons and the Einstein–de Haas effect. *Phys. Rev. Lett.* **112**, 085503 (2014).
8. Zhang, L. & Niu, Q. Chiral phonons at high-symmetry points in monolayer hexagonal lattices. *Phys. Rev. Lett.* **115**, 115502 (2015).
9. Zhu, H. et al. Observation of chiral phonons. *Science* **359**, 579 (2018).
10. Tauchert, S. R. et al. Polarized phonons carry angular momentum in ultrafast demagnetization. *Nature* **602**, 73 (2022).
11. Juraschek, D. M. & Spaldin, N. A. Orbital magnetic moments of phonons. *Phys. Rev. Mater.* **3**, 064405 (2019).
12. Schaack, G. Observation of circularly polarized phonon states in an external magnetic field. *J. Phys. C: Solid State Phys.* **9**, L297 (1976).
13. Schaack, G. Magnetic field dependent splitting of doubly degenerate phonon states in anhydrous cerium-trichloride. *Z. Phys. B* **26**, 49 (1977).
14. Mills, D. L. & Ushioda, S. Exciton–optical-phonon coupling in CoF_2. *Phys. Rev. B* **2**, 3805 (1970).
15. Cheng, B. et al. A large effective phonon magnetic moment in a Dirac semimetal. *Nano Lett.* **20**, 5991 (2020).
16. Baydin, A. et al. Magnetic control of soft chiral phonons in PbTe. *Phys. Rev. Lett.* **128**, 075901 (2022).
17. Ren, Y., Xiao, C., Saparov, D. & Niu, Q. Phonon magnetic moment from electronic topological magnetization. *Phys. Rev. Lett.* **127**, 186403 (2021).
18. Saparov, D., Xiong, B., Ren, Y. & Niu, Q. Lattice dynamics with molecular Berry curvature: chiral optical phonons. *Phys. Rev. B* **105**, 064303 (2022).
19. Hernandez, F. G. G. et al. Chiral phonons with giant magnetic moments in a topological crystalline insulator. Preprint at https://arxiv.org/abs/2208.12235 (2023).
20. Pimenov, A. et al. Possible evidence for electromagnons in multiferroic manganites. *Nat. Phys.* **2**, 97 (2006).
21. Sushkov, A. B., Aguilar, R. V., Park, S., Cheong, S. W. & Drew, H. D. Electromagnons in multiferroic YMn_2O_5 and $TbMn_2O_5$. *Phys. Rev. Lett.* **98**, 027202 (2007).
22. Katsura, H., Balatsky, A. V. & Nagaosa, N. Dynamical magnetoelectric coupling in helical magnets. *Phys. Rev. Lett.* **98**, 027203 (2007).
23. Valdés Aguilar, R. et al. Colossal magnon-phonon coupling in multiferroic $Eu_{0.75}Y_{0.25}MnO_3$. *Phys. Rev. B* **76**, 060404 (2007).
24. Valdes Aguilar, R. et al. Origin of electromagnon excitations in multiferroic $RMnO_3$. *Phys. Rev. Lett.* **102**, 047203 (2009).
25. Seki, S., Kida, N., Kumakura, S., Shimano, R. & Tokura, Y. Electromagnons in the spin collinear state of a triangular lattice antiferromagnet. *Phys. Rev. Lett.* **105**, 097207 (2010).
26. Takahashi, Y., Shimano, R., Kaneko, Y., Murakawa, H. & Tokura, Y. Magnetoelectric resonance with electromagnons in a perovskite helimagnet. *Nat. Phys.* **8**, 121 (2011).
27. Smolenskiĭ, G. A. & Chupis, I. E. Ferroelectromagnets. *Sov. Phys. Usp.* **25**, 475 (1982).
28. Le Page, Y. & Strobel, P. Structure of iron(II) molybdenum(IV) oxide $Fe_2Mo_3O_8$. *Acta Cryst.* **B38**, 1265 (1982).
29. Wang, Y. et al. Unveiling hidden ferrimagnetism and giant magnetoelectricity in polar magnet $Fe_2Mo_3O_8$. *Sci. Rep.* **5**, 12268 (2015).
30. Ideue, T., Kurumaji, T., Ishiwata, S. & Tokura, Y. Giant thermal Hall effect in multiferroics. *Nat. Mater.* **16**, 797 (2017).
31. Kurumaji, T. et al. Electromagnon resonance in a collinear spin state of the polar antiferromagnet $Fe_2Mo_3O_8$. *Phys. Rev. B* **95**, 020405 (2017).
32. Yu, S. et al. High-temperature terahertz optical diode effect without magnetic order in polar $FeZnMo_3O_8$. *Phys. Rev. Lett.* **120**, 037601 (2018).
33. Varret, F., Czeskleba, H., Hartmann-Boutron, F. & Imbert, P. Étude par effet Mössbauer de l'ion Fe^{2+} en symétrie trigonale dans les composés du type $(Fe, M)_2Mo_3O_8$ (M = Mg, Zn, Mn, Co, Ni) et propriétés magnétiques de $(Fe, Zn)_2Mo_3O_8$. *J. Phys. France* **33**, 549 (1972).
34. Csizi, B. et al. Magnetic and vibronic terahertz excitations in Zn-doped $Fe_2Mo_3O_8$. *Phys. Rev. B* **102**, 174407 (2020).
35. Squires, G. L. *Introduction to the Theory of Thermal Neutron Scattering* 3rd edn (Cambridge Univ. Press, 2012).

36. Bradley, C. & Cracknell, A. *The Mathematical Theory of Symmetry in Solids* (Oxford Univ. Press, 2009).
37. Anastassakis, E. & Burstein, E. Morphic effects. V. Time reversal symmetry and the mode properties of long wavelength optical phonons.*J. Phys. C: Solid State Phys.* **5**, 2468 (1972).

Methods

Crystal growth and INS

High-quality single crystals of $Fe_2Mo_3O_8$ were grown by the chemical vapour transport method using $TeCl_4$ as the transport agent, following the procedures detailed elsewhere[38,39]. The sample for the INS experiment was composed of approximately 150 pieces of single crystals weighing about 3.39 g in total. These single crystals were well co-aligned and glued onto four aluminium plates using backscattering Laue X-ray diffraction, resulting in an overall sample mosaic of less than 3°. The four plates were then assembled together on an aluminium holder, which can be mounted into a closed-cycle refrigerator for measurements. The neutron scattering measurements were performed at 4SEASONS, a time-of-flight spectrometer located at the Materials and Life Science Experimental Facility, J-PARC, Japan[40], under proposal no. 2020B0002. The neutron data were collected at 6 and 100 K, with an incident energy $E_i = 11.93$ meV and a chopper frequency of 250 Hz, resulting in an energy resolution of about 0.56 meV (full-width at half-maximum) at the elastic position.

Polarization-resolved magneto-Raman spectroscopy

In the magneto-Raman measurements, the samples were placed inside a cryogen-free superconducting magnet with the temperature range from 1.6 to 300.0 K. The magnetic fields up to 9 T were applied along the c axis of $Fe_2Mo_3O_8$ (Faraday geometry). A He–Ne laser (632.8 nm) with a power of 300 μW was utilized as the excitation light source. The excitation beam was focused on the sample by a non-magnetic objective with a beam size of 1 μm. The backscattered light was collected by the objective and it went through polarization optics and Raman filters. The Raman signals were then collected by a high-resolution spectrometer with LN_2-cooled charge-coupled device arrays. The spectral resolution is 0.3 cm^{-1}. For the cross-circular Raman configuration, zero-order half- and quarter-wave plates were used.

Phonon mode calculation

We use the generalized gradient approximation method implemented in the density functional theory (DFT) first-principles Vienna ab initio software package[41], where the electron–electron exchange correlation is described by the Perdew–Burke–Ernzerhof functional[42]. The all-electron projector augmented-wave method[43] was adopted, and the cut-off value of the plane-wave energy was 800 eV. In structural optimization, we use DFT+U to correct the Fe3d shell, where $U_d = 5$ eV and $J_d = 1$ eV. The geometric optimization converges with the convergence criteria of 1×10^{-3} eV Å^{-1} and 1×10^{-7} eV for force and energy per atom, respectively. The Brillouin zone is sampled in the Monkhorst–Pack[44] mode with a grid spacing of $2\pi \times 0.02$ Å^{-1}. Phonon spectrum calculations were performed using the PHONOPY package[45] with the finite displacement method (not considering magnetism), using a $2 \times 2 \times 1$ supercell, and used to identify the irreducible representation of the region-centric phonon modes.

Symmetry analysis of the phonon IR activity

We employ the theory of magnetic point groups and their co-representations to determine the IR activity of phonons[36,37]. Supplementary Information provides an exposition of the relevant background material and further details of the group theory analysis.

We first determine the magnetic point group associated with the AFM order. The crystalline point group of $Fe_2Mo_3O_8$ is C_{6v} ($6mm$), whose symmetry operations include a six-fold axis, a mirror plane (σ_v) that contains the six-fold axis and bisects the edge of a Fe hexagon and another mirror plane (σ_d) that contains the six-fold axis and the diagonal of the Fe hexagon. The AFM order reduces the six-fold axis to a three-fold axis, and destroys σ_d, indicating that the point group is C_{3v} ($3m$), an index-2 normal subgroup of C_{6v}. However, these symmetries can be partially restored if they are to be combined with a time-reversal operation Θ. Thus, the symmetry of the AFM phase is described by the magnetic point group $C_{3v} + \Theta(C_{6v} - C_{3v})$ or $6'm'm$ (ref. 36).

The phonons in the AFM phase are classified by the irreducible co-representations (coreps) of the magnetic point group. Also, $6'm'm$ admits three inequivalent, irreducible co-representations (irreps), which are in one-to-one correspondence to the irreps of C_{3v}. They are labelled as DA, DB and DE, in correspondence to the irreps A, B and E of C_{3v}, respectively. In particular, the P1 phonons, which carry the E_2 irrep of the point group $6mm$ in the paramagnetic phase, now carry the DE corep in the AFM phase.

We determine the IR-active coreps by decomposing the three-dimensional corep carried by the electric polarization vector. We find the in-plane (a–b) components of the polarization vector transform as DE. Thus, the P1 phonons are IR active in the a–b plane.

Finally, the same procedure shows that the symmetry of the FiM phase can be described by the magnetic point group $6'm'm'$, whose coreps are in one-to-one correspondence to the irreps of the point group C_6 (6). The P1 phonons now split into the coreps $DE_2^{(1)} + DE_2^{(2)}$, which are Raman active but not IR active.

Calculating PMM by perturbation theory

We calculate the PMM in two steps. In the first step, we write down the model Hamiltonian that describes the coupling between the P1 phonons and the zone-centre magnons. In the second, we compute the phonon Zeeman splitting due to the coupling and extract the effective magnetic moment.

Let Q_1 and Q_2 be the canonical coordinates of P1 phonons. As the P1 phonons carry the E_2 irrepresentation of the C_{6v} ($6mm$) point group, we require Q_1 and Q_2 transform as $\{\cos 2\phi, \sin 2\phi\}$ under the point group operations, where ϕ is the azimuthal angle in the crystallographic a–b plane. It is convenient for latter purposes to use the chiral basis: $Q_R = (Q_1 + iQ_2)/\sqrt{2}$ and $Q_L = (Q_1 - iQ_2)/\sqrt{2}$, which transform as $\{e^{2i\phi}, e^{-2i\phi}\}$. In the AFM phase, they carry the DE co-representation of the magnetic point group $6'm'm$.

In the AFM phase, $Fe_2Mo_3O_8$ hosts two pairs of doubly degenerate magnon modes at the zone centre. For the sake of simplicity, we focus on one degenerate pair; the other pair can be straightforwardly incorporated. As the magnons are also classified by the co-representations[36,37], the degenerate pair must carry the DE co-representation. Let α_R and α_L be the magnon annihilation operators for the two degenerate modes. We require that they transform as $\{e^{2i\phi}, e^{-2i\phi}\}$ under the magnetic point group operations. As a result, $\alpha_L^\dagger$ and $\alpha_R^\dagger$ also transform as $\{e^{2i\phi}, e^{-2i\phi}\}$.

The Hamiltonian for the magnon–phonon system is given by

$$H = \omega_m\left(\alpha_L^\dagger\alpha_L^\dagger + \alpha_R^\dagger\alpha_R^\dagger\right) + g\mu_B B\left(\alpha_L^\dagger\alpha_L^\dagger - \alpha_R^\dagger\alpha_R^\dagger\right) + \omega_0\left(c_L^\dagger c_L^\dagger + c_R^\dagger c_R^\dagger\right) - \sqrt{2}\gamma\left(Q_R\left(\alpha_L^\dagger + \alpha_R^\dagger\right) + Q_L\left(\alpha_R^\dagger + \alpha_L^\dagger\right)\right). \quad (1)$$

The first two terms describe the magnon modes and their Zeeman splitting in an external field B in the crystallographic c direction, ω_m is the magnon frequency, g is the Landé g-factor for the magnon and μ_B is the Bohr magneton. The third term describes the degenerate phonon modes. Here c_L and c_R annihilate a phonon with the left- and right-handed circular polarization, respectively. Also, $\omega_0 < \omega_m$ is the phonon frequency. The last term describes the linear coupling between the phonon and magnon; $Q_R = (c_R^\dagger + c_L^\dagger)/\sqrt{2}$ and $Q_L = (c_L^\dagger + c_R^\dagger)/\sqrt{2}$. The prefactor of $\sqrt{2}$ is for latter convenience.

We are now ready to compute the correction to the phonon frequency due to coupling. To this end, we consider the retarded Green's function of the phonons:

$$iG_{LR}^r(t) = \theta(t)\langle[Q_L(t), Q_R(0)]\rangle, \quad (2a)$$

$$iG_{RL}^r(t) = \theta(t)\langle[Q_R(t), Q_L(0)]\rangle. \quad (2b)$$

In particular, the positive-frequency part of Green's function G_{LR}^r probes the phonon with the left-handed circular polarization, whereas G_{RL}^r

probes the phonon with the right-handed circular polarization. The unperturbed Green's function, in the frequency domain, reads

$$G^{r}_{\mathrm{LR/RL},0}(\omega)=\frac{\omega_0}{(\omega+\mathrm{i}\epsilon)^2-\omega_0^2}\equiv g(\omega). \tag{3}$$

Here ϵ is an infinitesimal positive number. On including the interaction with magnons, Green's function is given by

$$G^{r}_{\mathrm{LR/RL}}(\omega)=\frac{1}{g^{-1}(\omega)-\Sigma_{\mathrm{RL/LR}}(\omega)}, \tag{4}$$

where $\Sigma_{\mathrm{RL/LR}}(\omega)$ is the self-energy. Note the subscripts of the Green function and the self-energy are switched—the correction to the 'LR' component of Green's function comes from the 'RL' component of the self-energy. Provided the self-energy correction is small, the renormalized phonon frequency is given by

$$\omega'_{\mathrm{L/R}}=\omega_0+\frac{1}{2}\mathrm{Re}\Sigma_{\mathrm{RL/RL}}(\omega_0). \tag{5}$$

We now set out to compute the self-energy; to the leading order in γ, it is given by

$$\Sigma_{\mathrm{RL/LR}}(\omega)=\frac{2\gamma^2}{\omega+\mathrm{i}\epsilon-(\omega_\mathrm{m}\pm g\mu_0 B)}-\frac{2\gamma^2}{\omega+\mathrm{i}\epsilon+(\omega_\mathrm{m}\mp g\mu_0 B)}, \tag{6}$$

where the top (bottom) sign is for the RL (LR) component. Thus, we find that the correction to the phonon frequency reads

$$\omega'_{\mathrm{L/R}}\approx\omega_0+\frac{\gamma^2}{\omega_0-\omega_\mathrm{m}\mp g\mu_0 B}, \tag{7}$$

where the top (bottom) sign is for the L/R component. We have omitted the subdominant contribution of ~$1/(\omega+\omega_\mathrm{m}\pm g\mu_0 B)$, which is justified when ω_0 is comparable with ω_m in magnitude.

We may extract the effective magnetic moment from the energy difference between the right- and left-handed circularly polarized phonons:

$$\frac{\mu_\mathrm{eff}}{\mu_\mathrm{B}}=\lim_{B\to 0}\frac{\omega_\mathrm{L}-\omega_\mathrm{R}}{2B}=g\left(\frac{\gamma}{\omega_0-\omega_\mathrm{m}}\right)^2. \tag{8}$$

This is the result given in the main text. When there are multiple magnon modes, we may straightforwardly extend the above result as

$$\frac{\mu_\mathrm{eff}}{\mu_\mathrm{B}}=\sum_i g_i\left(\frac{\gamma_i}{\omega_0-\omega_{\mathrm{m},i}}\right)^2, \tag{9}$$

where the sum is over all the degenerate magnon pairs. Also, g_i, γ_i and $\omega_{\mathrm{m},i}$ are the g-factor, coupling constant and magnon energy, respectively.

Minimal model for fluctuation enhancement in PMM

The minimal model consists of three pieces, namely, $H=H_\mathrm{spin}+H_\mathrm{phonon}+H_\mathrm{coupling}$. Here H_spin describes the spin degrees of freedom carried by the Fe ions. In light of the substantial easy-axis anisotropy of this material[29], we model it as an Ising magnet on an AA-stacked honeycomb lattice:

$$H_\mathrm{spin}=J\sum_{\langle ij\rangle\in ab}S_i^zS_j^z-J_c\sum_{\langle ij\rangle\in c}S_i^zS_j^z-g_1\mu_\mathrm{B}B\sum_{i\in\text{Fe-I}}S_i^z-g_2\mu_\mathrm{B}B\sum_{i\in\text{Fe-II}}S_i^z. \tag{10}$$

Here $S^z=\pm S$ are the Ising spins, where S is the spin quantum number ($S=2$ in $Fe_2Mo_3O_8$). The first summation is over all the nearest-neighbour pairs within the a–b plane, whereas the second is over the pairs in the c axis. $J>0$ and $J_c>0$ are the intra- and interlayer exchange interaction, respectively. Experiments suggest that the AFM state and FiM state are energetically competitive. We mimic this effect by choosing $J_c=0.01J$. We stress that such a choice does not mean that the microscopic exchange interactions between interlayer Fe ions are necessarily weak. It is probable that the interlayer interactions are frustrated. Here J_c should be understood as an effective interaction where the frustration effects have been subsumed. The last two terms of H_spin describe the Zeeman coupling. Here $g_{1,2}$ are the Landé g-factors of the Fe-I and Fe-II ions, respectively. Also, B is the field along the c axis. We choose $g_1=2.0$ and $g_2=2.4$ to match the measured g-factors of the magnons. We expect Fe-II ions to have the larger g-factors than Fe-I ions given their stronger spin–orbital coupling.

H_phonon describes the P1 phonons:

$$H_\mathrm{phonon}=\omega_0\left(c_\mathrm{L}^\dagger c_\mathrm{L}+c_\mathrm{R}^\dagger c_\mathrm{R}\right). \tag{11}$$

Here ω_0 is the bare phonon frequency; c_α ($c_\alpha^\dagger$) annihilates (creates) a phonon with polarization $\alpha=$ L, R. We require that c_R and c_L transform as $\{e^{2i\phi}, e^{-2i\phi}\}$ under the point group operations, where ϕ is the azimuthal angle in the a–b plane. We set the phonon frequency to be half of the magnon frequency ($3.0JS$), similar to the case with $Fe_2Mo_3O_8$: $\omega_0=1.5JS$.

Finally, H_coupling describes the coupling between the P1 phonons and spins:

$$H_\mathrm{coupling}=-\gamma^{(\mathrm{I})}\left(Q_\mathrm{L}O_\mathrm{R}^{(\mathrm{I})}+Q_\mathrm{R}O_\mathrm{L}^{(\mathrm{I})}\right)-\gamma^{(\mathrm{II})}\left(Q_\mathrm{L}O_\mathrm{R}^{(\mathrm{II})}+Q_\mathrm{R}O_\mathrm{L}^{(\mathrm{II})}\right). \tag{12}$$

Here $\gamma^{(\mathrm{I}),(\mathrm{II})}$ are the spin–phonon coupling constants. Q_L and Q_R are the phonon canonical coordinates, where $Q_\mathrm{L}=(c_\mathrm{L}+c_\mathrm{R}^\dagger)/\sqrt{2}$ and $Q_\mathrm{R}=(c_\mathrm{R}+c_\mathrm{L}^\dagger)/\sqrt{2}$. Also, $O^{(\mathrm{I})}_{\mathrm{L,R}}$ and $O^{(\mathrm{II})}_{\mathrm{L,R}}$ are bilinear spin operators, which transform in the same way as $\{Q_\mathrm{L}, Q_\mathrm{R}\}$ under the point group operations. They are given as follows:

$$O^{(\mathrm{I})}_{\mathrm{L/R}}=\frac{1}{\sqrt{N}}\sum_{i\in\text{Fe-I}}\sum_{j\in N_i}\eta_i S_i^\pm S_j^z, \tag{13a}$$

$$O^{(\mathrm{II})}_{\mathrm{L/R}}=\frac{1}{\sqrt{N}}\sum_{i\in\text{Fe-II}}\sum_{j\in N_i}\eta_i S_i^\pm S_j^z. \tag{13b}$$

The top (bottom) sign is for L (R). Also, $\eta_i=1$ (-1) if site i is in the even (odd) layers. The summation over j is restricted to the three nearest neighbours of site i in the same layer, N is the number of lattice unit cells and the prefactor of $1/\sqrt{N}$ is to ensure the correct thermodynamic limit. The O operators are constrained by the following requirements: (1) they are bilinear products of neighbouring spin operators in the same layer; (2) they carry the E_2 representation of the C_{6v} point group and are time-reversal invariant; (3) they must be able to induce a linear hybridization between the phonon and zone-centre magnons. Equation (13b) are the only choices. Physically, H_coupling describes the modification of the exchange interactions by lattice distortion. Here a Dzyaloshinskii–Moriya-like anisotropic exchange interaction—forbidden by the crystal point group symmetry—appears as the lattice distortion lowers the point group symmetry.

The ratio between the two independent coupling constants $\gamma^{(\mathrm{I})}$ and $\gamma^{(\mathrm{II})}$ cannot be determined a priori. Our simulation shows that choosing $\gamma^{\mathrm{I}}\gg\gamma^{\mathrm{II}}$ can produce the enhanced PMM near T_N. We, therefore, set $\gamma^{\mathrm{II}}=0$ and $\gamma^{\mathrm{I}}\neq 0$ for the sake of simplicity. Such an 'asymmetric' choice is not unexpected in that the atomic displacements of the P1 phonons are dominated by one of the two species of Fe ions (Fig. 1b), although the microscopic origin for such a coupling remains unclear at the moment. Interestingly, we note that the other limit, that is, $\gamma^{\mathrm{II}}\neq 0$ and $\gamma^{\mathrm{I}}=0$, would give rise to an enhanced PMM but with a negative sign. This striking phenomenon is worthy of further experimental exploration.

We calculate the PMM by using the many-body perturbation theory. Treating the spin–phonon coupling as a perturbation, we find the phonon self-energy is given by

$$\Sigma_{\mathrm{LR/RL}}(\omega) = \left(\gamma^{(\mathrm{I})}\right)^2 \chi^{(\mathrm{I})}_{\mathrm{RL/LR}}(\omega). \tag{14}$$

Here we have defined the response functions:

$$\mathrm{i}\chi^{(\mathrm{I})}_{\mathrm{LR}}(t) = \theta(t)\left\langle [O^{(\mathrm{I})}_{\mathrm{L}}(t), O^{(\mathrm{I})}_{\mathrm{R}}(t)]\right\rangle, \tag{15a}$$

$$\mathrm{i}\chi^{(\mathrm{I})}_{\mathrm{RL}}(t) = \theta(t)\langle [O^{(\mathrm{I})}_{\mathrm{R}}(t), O^{(\mathrm{I})}_{\mathrm{L}}(t)]\rangle. \tag{15b}$$

The parameter $\chi^{(\mathrm{I})}_{\mathrm{LR,RL}}$ encodes the spin fluctuations' impact on phonon dynamics. Owing to the simple form of the Hamiltonian, we may semi-analytically compute these response functions. The results are given by

$$\chi^{(\mathrm{I})}_{\mathrm{LR/RL}}(\omega) = \pm\frac{2}{N}\sum_{i\in\mathrm{Fe\text{-}I}}\left\langle \frac{T_i^2 S_i^z}{\omega + \mathrm{i}\epsilon \mp \Omega_i}\right\rangle. \tag{16}$$

Here the top (bottom) sign is for LR (RL). We have used a few short-hand notations to simplify the expression: $\langle\cdots\rangle$ denotes the statistical average with respect to the spin Hamiltonian H_{spin}. $T_i = \sum_{j\in N_i} S_j^z$ is the sum of the three neighbouring spins of site i in the same layer. $\Omega_i = -JT_i + J_c(S^z_{i+c} + S^z_{i-c}) + g_{1,2}\mu_0 B$ is the precessing frequency of the spin at i.

With the expression for self-energy at hand, we are now ready to write down the expression for the phonon frequency shift:

$$\omega'_{\mathrm{L/R}} = \omega_0 + \frac{\left(\gamma^{(\mathrm{I})}\right)^2}{2}\mathrm{Re}\chi^{(\mathrm{I})}_{\mathrm{LR/RL}}(\omega_0) = \omega_0 \pm \frac{\left(\gamma^{(\mathrm{I})}\right)^2}{N}\sum_{i\in\mathrm{Fe\text{-}I}}\left\langle \frac{T_i^2 S_i^z}{\omega_0 \mp \Omega_i}\right\rangle. \tag{17}$$

The quantity of interest is the phonon effective magnetic moment, which may be extracted as follows:

$$\mu_{\mathrm{eff}} = \frac{1}{2}\left(\frac{\partial\omega'_{\mathrm{L}}}{\partial B} - \frac{\partial\omega'_{\mathrm{R}}}{\partial B}\right)\Big|_{B=0} = \frac{\partial\omega'_{\mathrm{L}}}{\partial B}\Big|_{B=0}. \tag{18}$$

The second equality follows from the fact that the left-handed mode and right-handed mode symmetrically split in the limit $B \to 0$. This relation can also be verified by a direct calculation. We note the magnetic field B enters the expression of ω'_{L} in two different ways: explicitly, the field appears in the expression of the local spin precessing frequency Ω_i. This reflects the Zeeman effect of the magnons/paramagnons. Implicitly, the field appears in the Boltzmann weight of spin configurations and therefore can affect the statistical average. As a result, after taking the derivative, we find that the effective moment consists of two parts:

$$\mu_{\mathrm{eff}} = \mu_{\mathrm{hybrid}} + \mu_{\mathrm{fluc}}. \tag{19}$$

The first part is due to hybridization between the (para)magnon and phonon:

$$\frac{\mu_{\mathrm{hybrid}}}{\mu_{\mathrm{B}}} = \frac{g_1\left(\gamma^{(\mathrm{I})}\right)^2}{N}\sum_{i\in\mathrm{Fe\text{-}I}}\left\langle \frac{T_i^2 S_i^z}{\left(\omega_0 - \Omega_i\right)^2}\right\rangle_{B=0}. \tag{20a}$$

We see that its expression closely resembles the expression for the magnetic moment at $T = 0$. The second part, however, finds no analogue at zero temperature and is due to thermal fluctuations:

$$\frac{\mu_{\mathrm{fluc}}}{\mu_{\mathrm{B}}} = \frac{\left(\gamma^{(\mathrm{I})}\right)^2}{Nk_{\mathrm{B}}T}\sum_{i\in\mathrm{Fe\text{-}I}}\left\langle \frac{T_i^2 S_i^z}{\omega_0 - \Omega_i} M\right\rangle_{B=0}, \tag{20b}$$

where $M = g_1\sum_{i\in\mathrm{Fe\text{-}I}} S_i^z + g_2\sum_{i\in\mathrm{Fe\text{-}II}} S_i^z$ is the dimensionless total magnetization of the system. Intuitively, μ_{fluc} arises because the field B also modifies the molecular field experienced by the (para)magnons. This effect is small in the ground state but can be pronounced near the phase transition.

We compute μ_{hybrid} and μ_{fluc} by using the Markov chain Monte Carlo method. We use a system of $10 \times 10 \times 10$ unit cells subject to periodic boundary conditions. We sample the Boltzmann distribution by using the Wolff cluster update[46]. The statistical average that appears in the expression of μ_{hybrid} and μ_{fluc} is performed over 40 parallel Markov chains, each consisting of a sequence of 1,000 samples, with 1,000 Monte Carlo steps discarded between two successive samples.

In the Supplementary Information, we document how the model's behaviour depends on the choice of the parameters. We find a strong correlation between the presence of FiM fluctuations and the enhanced PMM near T_{N}. In particular, if we suppress the FiM fluctuations by setting $g_1 = g_2$ or using a large J_c, we find μ_{fluc} vanishes and no enhancement is observed.

Data availability

All data that support the plots within this paper and other findings of this study are available from the corresponding authors upon request. Source data are provided with this paper.

References

38. Strobel, P. & Le Page, Y. Growth and morphology of single crystals of hexagonal molybdates(IV) $M_2Mo_3O_8$ (M=Mn, Fe, Co, Ni). *J. Cryst. Growth* **61**, 329 (1983).
39. Strobel, P., Page, Y. L. & McAlister, S. P. Growth and physical properties of single crystals of $Fe^{II}{}_2Mo^{IV}{}_3O_8$. *J. Solid State Chem.* **42**, 242 (1982).
40. Kajimoto, R. et al. The Fermi Chopper Spectrometer 4SEASONS at J-PARC. *J. Phys. Soc. Jpn* **80**, SB025 (2011).
41. Kresse, G. & Furthmüller, J. Efficient iterative schemes for ab initio total-energy calculations using a plane-wave basis set. *Phys. Rev. B* **54**, 11169 (1996).
42. Perdew, J. P., Burke, K. & Ernzerhof, M. Generalized gradient approximation made simple. *Phys. Rev. Lett.* **77**, 3865 (1996).
43. Blöchl, P. E. Projector augmented-wave method. *Phys. Rev. B* **50**, 17953 (1994).
44. Monkhorst, H. J. & Pack, J. D. Special points for Brillouin-zone integrations. *Phys. Rev. B* **13**, 5188 (1976).
45. Togo, A., Oba, F. & Tanaka, I. First-principles calculations of the ferroelastic transition between rutile-type and $CaCl_2$-type SiO_2 at high pressures. *Phys. Rev. B* **78**, 134106 (2008).
46. Wolff, U. Collective Monte Carlo updating for spin systems. *Phys. Rev. Lett.* **62**, 361 (1989).

Acknowledgements

We thank J. Li, J. Liu, S. Yu and O. Tchernsyhyov for valuable discussions. We thank R. Kajimoto and M. Nakamura for their help in carrying out the INS experiment. This work was supported by the National Key Research and Development Program of China (grant nos. 2020YFA0309200, 2021YFA1400400 and 2022YFA1403800), the National Natural Science Foundation of China (grant nos. 11974396, 12225407, 12074174, 12125404, 11974162 and 11834006) and the Strategic Priority Research Program of the Chinese Academy of Sciences (grant no. XDB33020300), as well as the Fundamental Research Funds for the Central Universities. S.B. thanks the support from the China Postdoctoral Science Foundation via grant nos. 2022M711569 and 2022T150315 and Jiangsu Province Excellent Postdoctoral Program via grant no. 20220ZB5. The phonon calculations were carried out using supercomputers at the High Performance Computing Center of Collaborative Innovation Center of Advanced Microstructures, the high-performance supercomputing centre of Nanjing University.

Author contributions

Q.Z. conceived the project. S.B. grew the single crystals under the supervision of J.W. F.W. performed the magneto-Raman measurements and analysed the data under the supervision of Q.Z. S.B. and J.W. performed the INS measurements. Y.Wan. and J.Z. provided the theoretical analysis of the experimental data and performed the model calculations. Y.Wang. and J.S. performed the first-principles calculation of the phonon modes. Q.Z., Y.Wan. and F.W. wrote the manuscript with critical inputs from S.B., J.W. and all the other authors.

Competing interests

The authors declare no competing interests.

Additional information

Supplementary information The online version contains supplementary material available at https://doi.org/10.1038/s41567-023-02210-4.

Correspondence and requests for materials should be addressed to Jinsheng Wen, Yuan Wan or Qi Zhang.

Peer review information *Nature Physics* thanks the anonymous reviewers for their contribution to the peer review of this work.